PAPER

Check for updates

Towards advanced remediation: CuS/CdS Z-scheme heterojunction with accelerated charge-transfer for efficient photocatalytic degradation of trypan blue

Samina Kousar,[a] Mohamed Abdel Rafea,[b] Magdi E. A. Zaki,[c] M. Khairy,[c] Mohamed R. El-Aassar,[d] Abdullah K. Alanazi,[e] Imran Shakir,[f] Sidra Mubeen*[g] and Muhammad Aadil ⓘ *[h]

This study involves the preparation of virgin CuS and CdS for comparative analysis, followed by the synthesis of a CuS/CdS heterojunction nanocomposite using co-precipitation and subsequent annealing. The structural and compositional investigations (XRD, FTIR, SEM, and EDX) verified high purity and the successful production of a heterojunction with hexagonal crystal phases. Characterization of electrical (I–V), optical (UV-Vis), and optoelectronic (photocurrent) properties demonstrated enhanced charge separation, a reduced band gap (2.52 eV), and augmented visible-light absorption in the composite. In comparison to its equivalents, the CuS/CdS exhibited significantly enhanced electrical conductivity (3.60×10^{-4} S m^{-1}), facilitating reduced recombination and accelerated charge transfer. The efficacy of the photocatalytic process was assessed using trypan blue, a stable commercial azo dye. The dye was completely eliminated by the CuS/CdS composite in 48 minutes through photocatalytic degradation (81%) and 15 minutes through adsorption (19%). The kinetic rate constant of 0.039 min^{-1} was 2.79 and 1.86 times greater than that of CdS and CuS, respectively. Post-cycle XRD analysis confirmed structural stability, and reusability studies over six cycles indicated an efficiency decrease of only 2.3%. The scavenger experiments indicated that superoxide radicals ($^{\bullet}O_2^{-}$) exhibited the highest reactivity among the species tested. Calculations of band edge potential have verified that the Z-scheme charge transfer mechanism facilitates efficient charge separation and the generation of reactive oxygen species (ROS). Curiously, the pH of the heterogeneous composite was found to be correlated with its photocatalytic activity. An examination of the pH level disclosed a PZC value of 5.39. The composite functioned most effectively at a pH of 4. A novel CuS/CdS composite has been explored that is not only novel but is also ecological, cost-effective, and structurally stable in mineralizing the persistent azo dyes.

1. Introduction

Industrial growth plays a pivotal role in sustaining human needs and economic stability. Nonetheless, industries such as textile, leather, paper, plastic, printing, cosmetic, and food processing are major contributors to the widespread release of synthetic dyes into water resources.[1] Due to their complex aromatic and azo structures, these dyes exhibit strong chemical stability, rendering them non-biodegradable and long-lasting contaminants that hinder light diffusion and limit the aquatic productivity, particularly by affecting phytoplankton-driven photosynthesis that maintains the oxygen–carbon dioxide balance. Established treatment methods generally underperform, either by redistributing pollutants or by achieving only partial degradation. Traditional water treatment approaches such as adsorption, coagulation–flocculation, membrane filtration, ion exchange, and biological oxidation have been extensively used; however, they usually achieve only partial dye removal and may create secondary waste streams.[2,3] Therefore, semiconductor photocatalysis has been recognized as a viable, solar-powered approach for transforming such pollutants into simpler and less toxic compounds.[4–7]

[a]Department of Chemistry, Govt. Sadiq Egerton Graduate College, Bahawalpur 63100, Pakistan

[b]Imam Mohammad Ibn Saud Islamic University (IMSIU), College of Science, Department of Physics, Riyadh 11623, Saudi Arabia

[c]Imam Mohammad Ibn Saud Islamic University (IMSIU), College of Science, Department of Chemistry, Riyadh 11623, Saudi Arabia

[d]Department of Chemistry, College of Science, Jouf University, PO Box 2014, Sakaka, Aljouf, Saudi Arabia

[e]Department of Chemistry, College of Science, Taif University, Taif, Saudi Arabia

[f]Department of Physics, Faculty of Science, Islamic University of Madinah, Madinah 42351, Saudi Arabia

[g]Department of Chemistry, The Women University Multan, Multan, 60000, Pakistan. E-mail: sidra.mubeen@wum.edu.pk

[h]Department of Chemistry, The Islamia University of Bahawalpur, Rahim Yar Khan Campus, Rahim Yar Khan 64200, Pakistan. E-mail: Muhammad.aadil@iub.edu.pk

Transition metal sulfides, among visible-light-responsive semiconductors, have drawn particular attention due to their adjustable band gaps, suitable band-edge positions, and outstanding carrier mobility.[8] Cadmium sulfide (CdS), an n-type semiconductor with a band gap of around 2.4 eV,[9] can efficiently utilize visible light but suffers from fast electron–hole recombination and severe photocorrosion during prolonged irradiation.[10] Copper sulfide (CuS), in contrast, is a p-type semiconductor with strong visible absorption and high hole mobility.[11] The combination of CuS and CdS to form a heterojunction can significantly improve charge separation efficiency and photostability through interfacial electron–hole migration. In particular, Z-scheme or S-scheme heterojunctions have proven superior to conventional type-II systems because they preserve the strong redox ability of the constituent semiconductors while still facilitating charge separation.[12,13] In a Z or S-scheme configuration, photogenerated electrons in the conduction band of the oxidation photocatalyst recombine with holes in the valence band of the reduction photocatalyst, leaving behind highly energetic electrons and holes with strong reduction and oxidation capacities.[14,15] This unique and co-supportive configuration promotes the interfacial charge transfer and hinders the unwanted back charge transfer; hence, enhanced photocatalytic activity and stability are achieved. Several studies recently have substantiated the advantage of Z-scheme systems, revealing their higher visible-light degradation capability and improved structural durability relative to type-II heterojunctions.[16,17]

Despite the extensive reporting of sulfide-based heterojunctions, the resolution of their underlying mechanisms is still incomplete. Most existing works employ cationic dyes such as methylene blue and rhodamine B,[18] whereas anionic azo dyes like trypan blue (TB) have received comparatively little attention. In several studies, the term "removal efficiency" is used ambiguously, with little distinction between dye adsorption and genuine photocatalytic mineralization, thereby complicating performance interpretation. Surface electrostatics, such as the point of zero charge (PZC) and pH-dependent surface potential, are frequently neglected, although they play a decisive role in controlling interfacial charge transfer and adsorption–reaction behavior.[19] Moreover, improvements in charge separation within photocatalytic systems are often inferred indirectly from enhanced degradation performance or spectral shifts, rather than substantiated through quantitative methods such as current–voltage ($I–V$) and photocurrent analyses that directly assess carrier transport behaviour. Lastly, in addition, the mechanistic interpretation of these composites remains unsettled, with inconsistent labelling as type-II or Z-scheme systems often made without rigorous validation from band-edge or scavenger-based experiments.[20] Aforementioned research gaps form the basis for this study, which aims to synthesized the CuS/CdS direct Z-scheme p–n heterojunction with experimentally corroborated mechanistic insight.

Herein, a well-coupled CuS/CdS heterostructure with Z-scheme-mediated interfacial synergy was prepared using a straightforward co-precipitation approach followed by mild annealing at low temperature. The resulting material showed enhanced photon capture and charge mobility and was applied to the visible-light degradation of trypan blue as a model contaminant. Structural, optical, and electrochemical characterizations confirmed the formation of a stable Z-scheme heterojunction capable of efficient charge separation and retention of strong redox potentials. The present study provides several distinctive contributions. Firstly, the CuS/CdS p–n heterostructure was deliberately engineered to promote efficient charge separation and suppress recombination, addressing a long-standing limitation of single-component sulfide photocatalysts. Secondly, trypan blue, a challenging anionic azo dye, was selected as a model pollutant to evaluate photocatalytic activity, with electrostatic pH and PZC analyses distinguishing adsorption from actual degradation. Thirdly, electrical conductivity and transient photocurrent tests quantitatively verified faster charge transfer across the CuS/CdS interface, demonstrating efficient carrier mobility. Fourthly, the direct Z-scheme charge-transfer mechanism was supported by solid mechanistic evidence from band-edge potential measurement and radical scavenger analysis. In this mechanism, CdS electrons and CuS holes operate in synergy to facilitate the redox reaction. Finally, the photocatalyst exhibited outstanding stability and reproducible activity upon multiple runs, demonstrating its potential in sustainable wastewater treatment. In summary, this study sets up the CuS/CdS heterostructure in the modern context of interfacially engineered photocatalysts where charge-transfer channels are optimized and experimentally confirmed. Directly addressing photocorrosion and recombination problems, it moves closer to the development of stable sulfide-based Z-scheme photocatalysts for environmentally benign applications.

2. Experimental section

2.1. Chemicals

All chemicals used were of analytical grade and utilized without further purification. Cadmium nitrate tetrahydrate ($Cd(NO_3)_2$·$4H_2O$), copper(II) acetate monohydrate ($Cu(CH_3COO)_2$·H_2O), thiourea ($(NH_2)_2CS$), and potassium hydroxide (KOH) were purchased from Sigma-Aldrich. Deionized water was used throughout the experiment for solution preparation, washing, and dilution processes.

2.2. Synthesis of CuS/CdS heterojunction

For the synthesis of the CuS/CdS heterostructure, 50 mL of 0.05 M aqueous solution of $Cd(NO_3)_2$ was heated to 70 °C under stirring. Then 50 mL of 0.05 M aqueous solution of $Cu(CH_3COO)_2$ was added to obtain an equimolar Cd^{2+}/Cu^{2+} mixture (Cu : Cd = 1 : 1). After 30 min, an aqueous thiourea solution (in excess; e.g., ≥2 equiv. vs. total metal ions) was introduced dropwise. The solution colour shifted from blue to dirty green (Cu^{2+}–thiourea complex formation). While maintaining 70 °C and vigorous stirring, 1 M KOH was added dropwise to adjust pH to 10–11. At this pH, thiourea decomposes to supply S^{2-}, and a dark brown-black precipitate of CuS/CdS is formed. The suspension was aged 60 min at temperature. The solid was

allowed to settle, the supernatant decanted, and the precipitate washed repeatedly with deionized water (to neutral pH) and ethanol, then vacuum-filtered and dried at 80 °C for 10 h. The dry powder (~1 g) was annealed under N_2 (preferred) at 400 °C for 3 h (ramp 2–5 °C min^{-1}) to enhance crystallinity and interfacial contact, then cooled naturally to room temperature. For comparison, pristine CdS and CuS were synthesized under identical conditions using only the respective metal precursor with thiourea and KOH, keeping all other parameters unchanged. The schematic illustration given in Fig. 1 visually summarizes the step-by-step procedure for the synthesis of CuS/CdS composite photocatalysts, highlighting the key stages involved in the preparation process.

2.3. Photocatalytic experiment

The photocatalytic performance of pristine CuS, CdS, and their composite CuS/CdS was assessed against the trypan blue dye. 20 mg of each catalyst was added into the 50 mL aqueous solution (15 ppm) of trypan blue separately. The obtained catalyst–dye solutions were stirred in the dark for 120 minutes/2 h to reach adsorption–desorption equilibrium. The initial absorbance of the catalyst–dye mixture was measured at 607 nm using a UV-Vis spectrophotometer to assess the amount of dye removal by physical adsorption onto the photocatalyst surface. Next, catalyst–dye suspensions were exposed to a visible-light tungsten lamp (LS-150/cm^2) installed at a distance of 10 cm from the photoreactor. Throughout the 48 minute light irradiation period, 5 mL aliquots of the catalyst–dye mixture were extracted at 6 minute intervals and centrifuged. The dye concentration was monitored over time by analyzing the resultant supernatants with a double-beam UV-visible spectrophotometer at 607 nm. The percentage degradation of the TBD in the case of each catalyst was determined using the following equations.[21]

$$\text{Removal (\%)} = \frac{C_0 - C_t}{C_0} \times 100 \qquad (1)$$

'C_0' and 'C_t' in this equation stand for the dye's starting concentration and the concentration measured at time 't', respectively.

3. Results and discussion

3.1. Structural study

XRD analysis was conducted to investigate the phase composition and chemical purity of CuS, CdS, and the synthesised CuS/CdS nanocomposite. Fig. 2a depicts the XRD patterns for CuS, CdS, and CuS/CdS.

The XRD pattern of virgin CuS shows strong peaks at 2θ values of 27.0°, 27.7°, 29.3°, 31.7°, 33.1°, 38.6°, 48.0°, 52.8°, and 59.3°, which correspond to the (100), (101), (102), (103), (006), (105), (110), (108), and (116) planes, respectively. These peaks are consistent with JCPDS card no. 79-2321, demonstrating the hexagonal crystalline phase of CuS.[22] The XRD pattern of CdS shows strong peaks at 2θ values of 26.8°, 30.6°, 43.9°, 52.1°, and 64.0°, which match the (111), (200), (220), (311), and (400) planes, confirming the hexagonal wurtzite phase according to JCPDS card no. 75-1546.[23] No unexpected peaks were observed in the XRD spectra of CuS and CdS, indicating pure phase formation without any secondary products.[24] The XRD pattern of the CuS/CdS composite exhibits distinct diffraction peaks for both CuS and CdS, hence affirming the effective integration and retention of their respective crystalline structures.[25] At the same time, minor changes in peak positions may be ascribed to physical interactions at the CuS–CdS interface.[26]
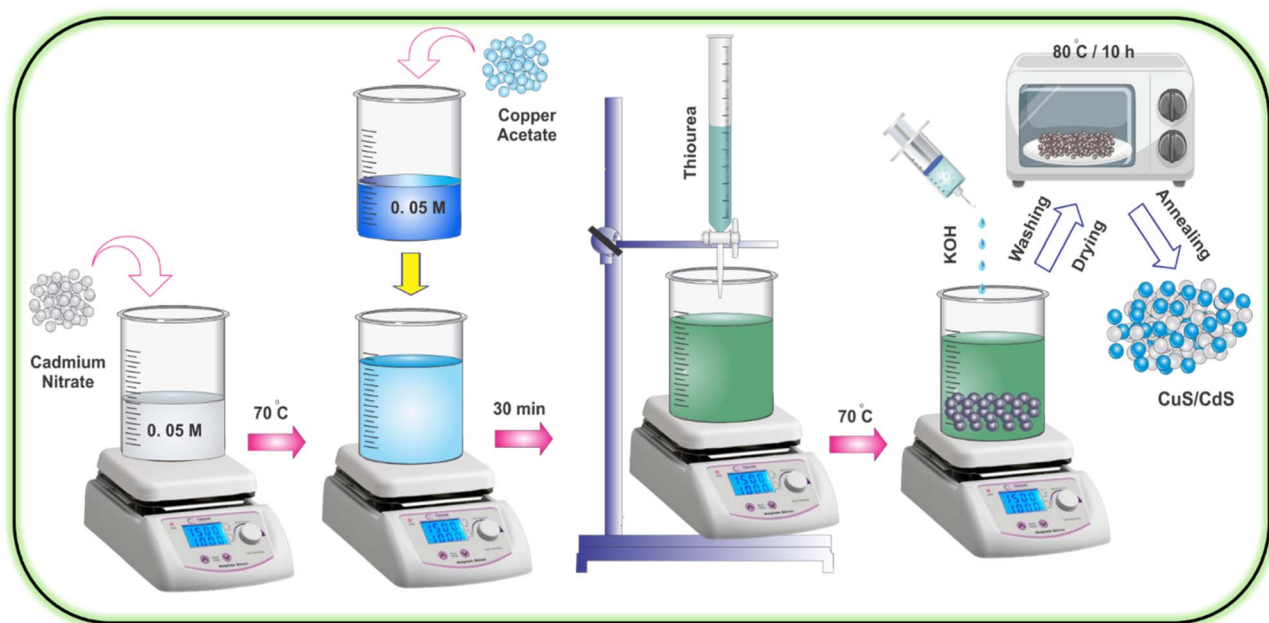

Fig. 1 Schematic representation of the synthesis procedure for CuS/CdS composite photocatalysts.
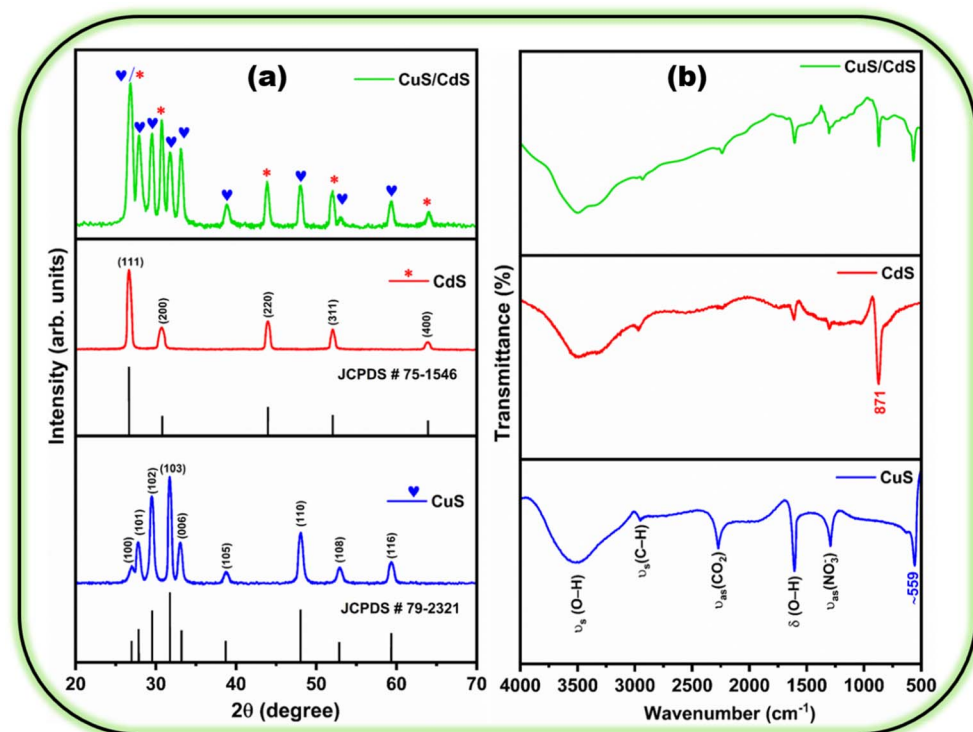
Fig. 2 Structural study: (a) XRD and (b) FTIR spectra of CuS, CdS, and the CuS/CdS.

The bonding properties and functional groups in the pure CuS, pristine CdS, and their composite CuS/CdS were investigated using FTIR spectroscopy. Fig. 2b presents the FTIR spectra of the synthesized materials recorded in the wavenumber range of 4000–500 cm^{-1}. CuS spectra showed a broad absorption band at 3509 cm^{-1} and a peak at 1605 cm^{-1}, indicating the presence of surface-adsorbed water molecules.[27,28] The transmittance at 2239 cm^{-1} is attributed to adsorbed ambient CO_2.[29] The absorption bands at 2953 cm^{-1} and 1302 cm^{-1} represent C–H vibrational modes and NO_3^- stretching vibrations, respectively, showing the existence of residual organic molecules and nitrate species.[30–32] The FTIR of CdS, apart from the characteristics bands of sorbed and residual chemical moieties, exhibits a prominent band at 559 cm^{-1} that corresponds to the Cu–S bond vibrations.[33] The FTIR spectrum of the CuS/CdS composite exhibits all characteristic peaks of both CuS and CdS, confirming the successful incorporation of both phases. The absence of significant peak shifts and the lack of additional peaks suggest that the structural integrity and purity of the CuS/CdS composite were preserved, in agreement with XRD results.

3.2. Morphological and elemental analyses

TEM characterization offered crucial insights into the microstructural arrangement and phase interaction of the CuS/CdS sample. As seen in the low-magnification TEM image (Fig. 3a), the sample consists of densely packed nanoparticles varying from 40 to 70 nm, forming a tightly interconnected network. The darker regions, marked with red-line, correspond to CdS

domains, which appear darker because of their higher atomic number and greater electron-scattering ability. In contrast, the brighter areas, marked with blue-line, represent CuS domains. The high-magnification image (Fig. 3b) reveals coherent particle boundaries and intimate contact, indicative of strong interfacial bonding across the heterojunction. Fig. 3c and d illustrate sharp CuS–CdS boundaries, visually proving nanoscale heterojunction formation that ensures efficient electron transfer along the Z-scheme pathway.

The elemental composition of the CuS/CdS composite was analyzed using EDX. The EDX spectrum (Fig. 4a) of the CuS/CdS composite verified the existence of Cu, Cd, and S elements, with three peaks at 0.9 keV, 8 keV, and 8.9 keV attributed to copper. The distinct peaks at around 3.1 keV and 3.3 keV indicate the presence of cadmium. The peak at 2.31 keV validated the existence of the S element.[34,35] The quantitative data in the EDX spectrum inset revealed atomic percentages of 26.59% for Cu, 24.58% for Cd, and 48.83% for sulfur. The findings, aligning with stoichiometric predictions, validated the effective synthesis of the composite with a 1 : 1 ratio of CuS to CdS. Furthermore, the lack of any further peak confirmed the purity of the synthesized composite.[36]

SEM-EDX mapping (Fig. 4b–d) was employed to further investigate the compositional homogeneity and interfacial distribution of elements within the CuS/CdS heterojunction. The overlay image (Fig. 4b) distinctly displays the coexistence of Cu (blue), Cd (green), and S (magenta), indicating uniform elemental intermixing and intimate interfacial contact between both sulfide phases. The individual Cu and Cd elemental maps
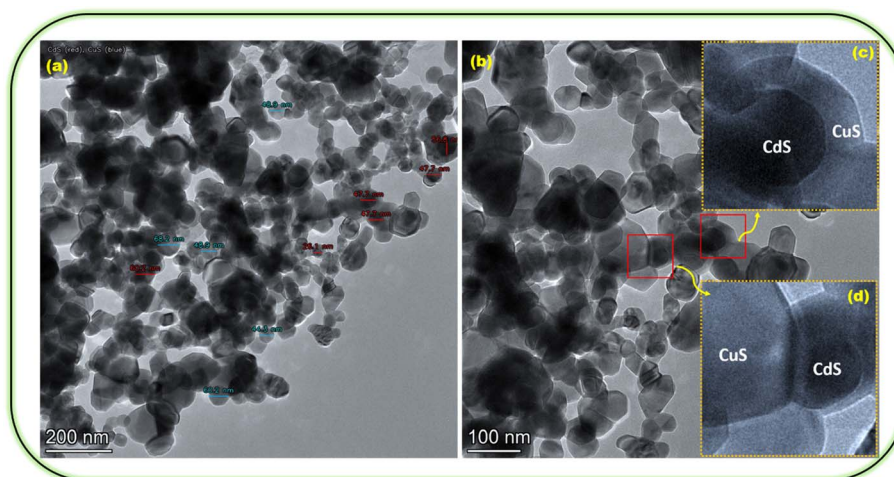
Fig. 3 TEM images of the CuS/CdS: (a) low-magnification view; (b) higher magnification revealing coherent interfaces; (c and d) enlarged junctions highlighting distinct CuS–CdS boundaries.
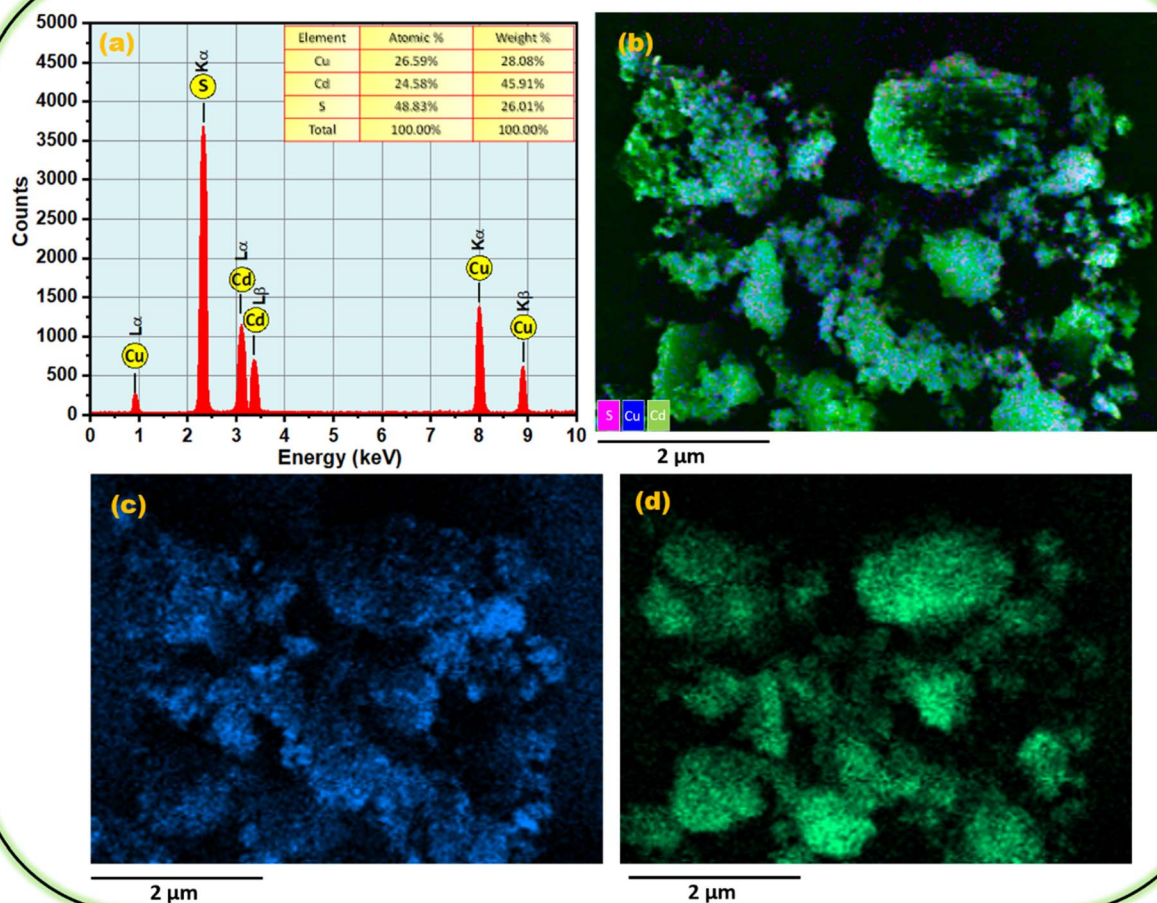

Fig. 4 SEM-EDX analysis of the CuS/CdS: (a) EDX spectrum confirming the presence of Cu, Cd, and S with corresponding elemental ratios; (b) elemental overlay map; and (c and d) individual Cu and Cd maps.

(Fig. 4c and d) reveal smooth and even dispersion across the matrix, confirming strong interfacial coupling and the successful formation of the CuS/CdS heterojunction. Since sulfur is common to both sulfides and uniformly distributed, its mapping was not shown separately.

3.3. Current–voltage study

To understand how well charges, move in our materials, we studied the electrical conductivity of CuS, CdS, and their composite (CuS/CdS) using current–voltage (I–V) measurements across a voltage range of −5 V to +5 V (Fig. 5a).

Among the three, CdS showed a curved I–V line with a very gentle slope, which points to weak charge mobility and poor electrical contact—both of which can limit its performance as a standalone photocatalyst. CuS, on the other hand, showed a more linear response and a steeper slope, indicating better electrical conductivity and charge transport.[37] Interestingly, the CuS/CdS composite displayed the most linear I–V curve and the highest slope, clearly reflecting a major improvement in conductivity. The absolute electrical conductivity (AEC) values for all three samples were precisely calculated using following relation.[38]

$$AEC = \frac{w \times slope}{A} \quad (2)$$

Here, 'w' and 'A' are the sample pellet's thickness and area respectively. Fig. 5b presents the computed AEC values for CdS, CuS, and CuS/CdS as 4.45×10^{-5} S m^{-1}, 1.91×10^{-4} S m^{-1}, and 3.60×10^{-4} S m^{-1}, respectively. Due to the fact that rapid and efficient charge transfer causes the reaction to occur more quickly, the greater AEC of CuS/CdS is considered to be essential for photocatalytic applications.[39] It is quite probable that the combination of CuS and CdS will perform more effectively in photocatalytic degradation processes, which makes it an excellent candidate for use in the process of cleaning up the environment.

3.4. Optical and opto-electronic study

UV-visible spectroscopy was utilized to evaluate the optical absorption properties of pure CuS, CdS, and their composite CuS/CdS. Fig. 6a illustrates the UV-Vis absorption spectra and the corresponding Tauc graphs for all three synthesized materials. The absorption spectrum of CuS exhibited strong absorption in the UV region and minimal absorption in the visible region up to 480 nm. Similarly, CdS revealed strong absorption in the UV region, with the absorption edge extended up to 500 nm in the visible region. The CuS/CdS composite exhibited improved and broadened absorption in the visible region, thereby enhancing its visible light harvesting ability. Synergistic interaction and effective heterojunction formation between CuS and CdS are responsible for this red shift in absorption. The optical band gap values of the produced nanocatalysts were ascertained using Tauc plot analysis utilizing the subsequent relation:[40]

$$(\alpha h\nu)^2 = K(h\nu - E_g) \quad (3)$$

where 'α' indicates the absorption coefficient, '$h\nu$' photon energy, 'E_g' band gap energy, 'K' constant, and $n = 1/2$ direct allowed transition. The estimated band gap energies were determined to be 2.76 eV, 2.9 eV, and 2.52 eV for CuS, CdS, and the CuS/CdS composite, respectively, as illustrated in the insets of Fig. 6a. In brief, the reduced band gap of the composite compared to its pristine components results in enhanced visible-light absorption, thereby boosting its photocatalytic efficiency.

Photocurrent analysis was utilized to investigate the photoelectrochemical behaviour and charge separation efficiency of the synthesized catalysts under visible light illumination.[41] The photocurrent response to 60-light-on/off cycles is shown in Fig. 6b. Pristine CuS, CdS, and their composite CuS/CdS showed a rapid photocurrent density spike upon light illumination that lasted 60 seconds before decreasing quickly to
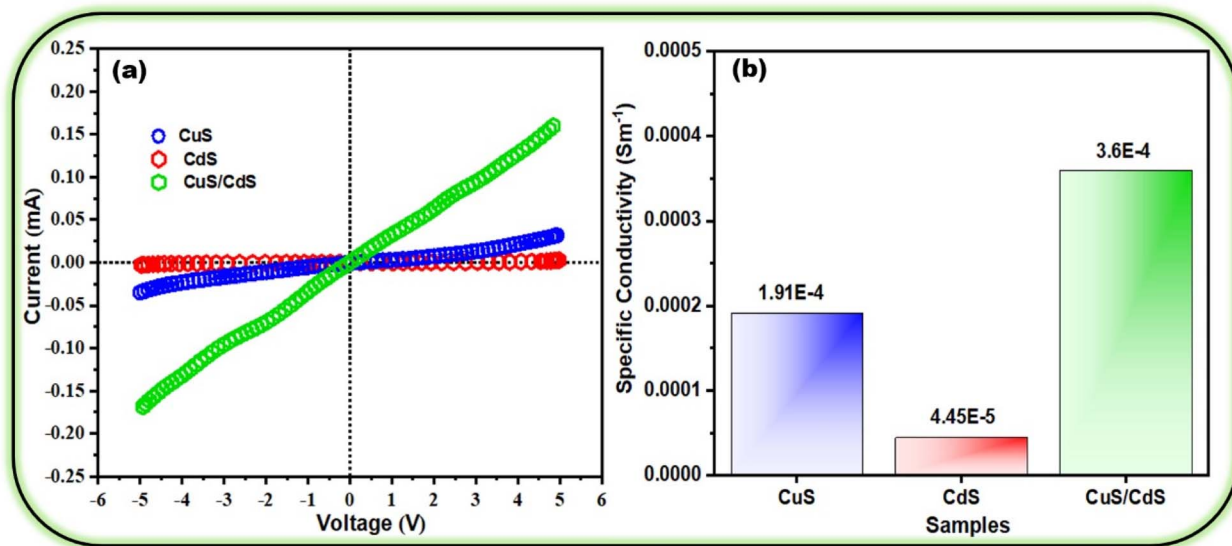

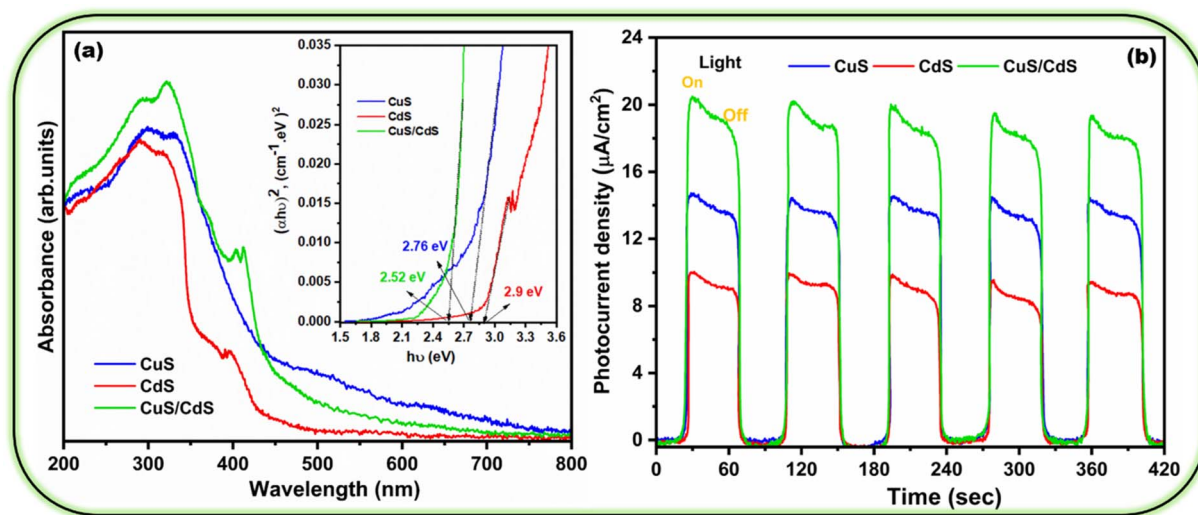**Fig. 5** (a) I–V plots and (b) AEC of CuS, CdS and CuS/CdS.

Fig. 6 (a) UV-Vis spectra, Tauc plot (inset) and (b) transient photocurrent response for CuS, CdS, and CuS/CdS.

zero when the light was turned off. Peak photocurrent density values were 20 μA cm^{-2} for CuS/CdS, 13 μA cm^{-2} for CuS, and 9 μA cm^{-2} for CdS. The improved and consistent photocurrent density response of CuS/CdS is attributed to the establishment of a Z-type heterojunction, which facilitates charge separation.[42,43] The synergistic interaction between CuS and CdS also amplifies visible light absorption. Moreover, the uniformity in photocurrent density during several light-on-off switching cycles validates the photostability and durability of the CuS/CdS heterostructure.[44]

3.5. Photocatalytic activity

The trypan blue dye-targeted photocatalytic degradation efficiency of pure CuS, CdS, and CuS/CdS was examined under visible light irradiation. After preparing a 15 ppm aqueous solution of trypan blue, each photocatalyst was dispersed into the dye solution separately, and the resulting catalyst–dye suspensions were stirred in darkness for 120 minutes/2 h for the establishment of adsorption–desorption equilibrium. Once the catalyst–dye solutions achieved adsorption–desorption equilibrium, UV-Vis spectra were captured in the 200–800 nm range. The elimination of trypan blue dye was assessed by tracking the drop-in absorbance at 607 nm. Fig. 7a–c presents the photodegradation activity of the nanocatalysts against the trypan blue dye.

CuS exhibited an adsorption of 13.6%, CdS reached an adsorption efficiency of 10.2%, while the CuS/CdS composite achieved an adsorption potential of 19%. The superior dye adsorption capacity of CuS/CdS compared to its pristine components is attributed to its improved surface-to-volume ratio and interfacial synergy between CuS and CdS. After that, catalyst–dye suspensions were kept on constant stirring under visible light irradiation for 48 minutes. The UV-Vis absorption spectra of small aliquots taken from the catalyst–dye suspension was recorded at regular intervals of 6 minutes. The incremental decrease in absorbance at 600 nm over the 48 minute

cumulative irradiation period indicated the gradual degradation of trypan blue dye. CuS and CdS exhibited dye degradation efficiencies of 61.3% and 46.3%, respectively, but the CuS/CdS composite achieved an 81% degradation after 48 minutes of exposure to visible light. The composite's improved photocatalytic effectiveness results from its extended visible light absorption and the establishment of a Z-type heterojunction between CuS and CdS, which effectively mitigates charge carrier recombination.[45]

The overall TBD dye removal efficiencies for CuS, CdS, and CuS/CdS nanocatalysts are presented in the bar chart (Fig. 7d), providing a clear comparison of their adsorption and photocatalytic performances. CuS removed 74.9% of the dye (13.6% adsorption and 61.3% photodegradation), CdS removed 56.5% (10.2% adsorption and 46.3% photodegradation), and the CuS/CdS composite removed all of it (100%), with 19% adsorption and 81% photodegradation. These results demonstrate the superior photocatalytic efficiency of the CuS/CdS composite.

Fig. 8a shows TBD dye concentration (C_t/C_0) fluctuations with irradiation duration for the control (no catalyst), CuS, CdS, and CuS/CdS photocatalysts. The TBD dye is highly photostable, as shown by its 2.3% decolorization in visible light for 48 minutes without a catalyst. CuS/CdS composite had the best photocatalytic performance, followed by pure CdS and CuS. Various kinetic models were employed to evaluate the kinetics of trypan blue degradation under visible light irradiation using CuS, CdS, and CuS/CdS nanocatalysts.

The pseudo-first-order model was the most effective in fitting the degradation data, as evidenced by a high adjusted R^2 value of 0.99 for all three catalysts. The following equation represents the pseudo-first-order kinetic model:[46]

$$kt = -\ln \frac{C_t}{C_0} \tag{4}$$

The rate constant values for each catalyst were determined by the slope obtained from the linear fitting of the $-\ln \quad C_t/C_0$
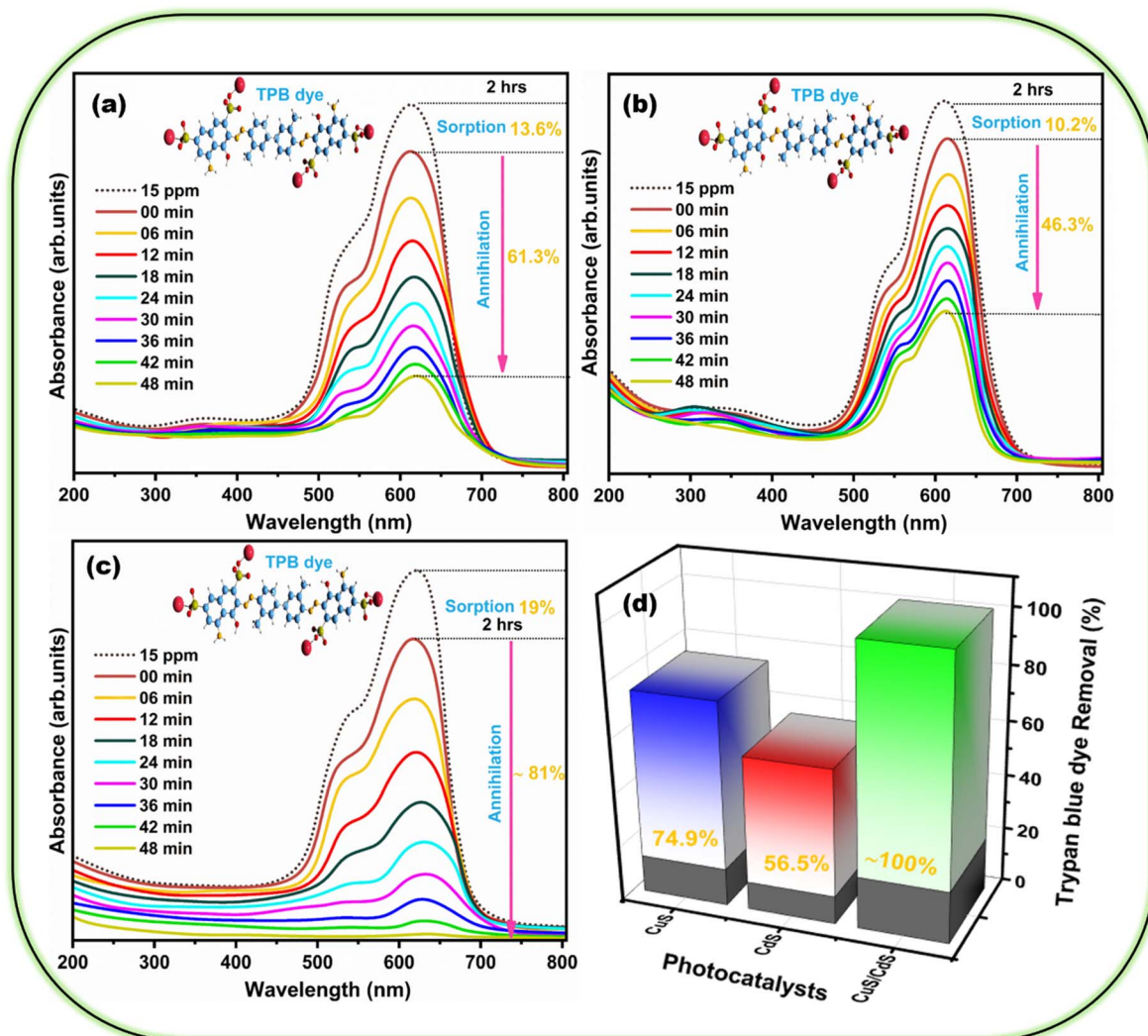
Fig. 7 Time resolved UV-Vis spectra for TBD degradation over (a) CuS, (b) CdS, (c) CuS/CdS, and (d) removal efficiency of each photocatalysts.
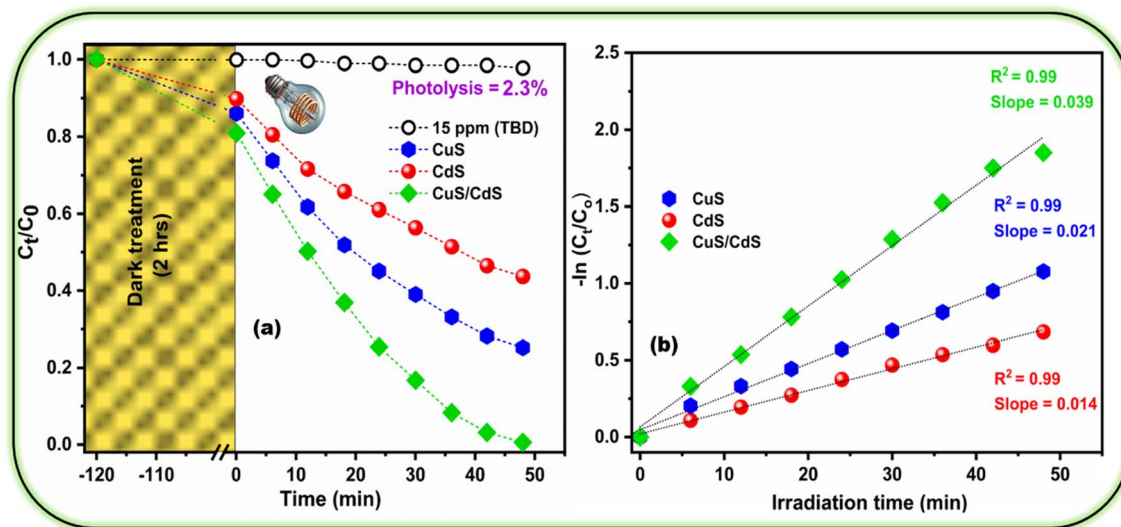

Fig. 8 (a) C_t/C_0 vs. time and (b) $-\ln C_t/C_0$ vs. time plot showing the TBD removal kinetics by CuS, CdS and CuS/CdS catalysts.

vs. time (min) plot. The observed rate constant for the CuS/CdS composite ($0.039 \ min^{-1}$) was 2.79 times greater than that of CdS ($0.014 \ min^{-1}$) and 1.86 times more than that of CuS ($0.021 \ min^{-1}$), as seen in Fig. 8b.

3.6. Measurement of PZC and effect of pH

The zeta potential analysis was used to determine the point of zero charge (PZC) for the CuS/CdS composite. PZC of the CuS/CdS composite was found to be 5.39, as shown in Fig. 9a. It means the catalyst carries a positive charge surface below PZC and a negative charge surface above this pH. The impact of pH on the rate constant of photocatalytic degradation efficiency of TBD is shown in Fig. 9b. The highest rate constant value of $0.039 \ min^{-1}$ was recorded at pH 4, due to the strong electrostatic attraction between the positively charged photocatalyst and anionic dye molecules, facilitating dye absorption and degradation. The rate constant value decreased above PZC and reached a minimum value of $0.007 \ min^{-1}$ at pH 7, which can be attributed to the repulsive forces between the negatively charged catalyst surface and the anionic dye, thereby reducing dye adsorption ability. On the other hand, under strongly acidic conditions (pH < 4), a decline in the rate constant value was observed, which can be attributed to the presence of excessive H^+ ions that saturate adsorption sites by protonating active sites, thereby reducing dye absorption.

3.7. Reusability and stability

The efficacy of photocatalysts is attributed to their reusability and photostability; hence, these characteristics of the CuS/CdS composite were examined through the photodegradation of trypan blue (15 ppm) in visible light. The photodegradation of trypan blue dye was examined during six cycles, each lasting 48 minutes. The catalyst obtained by centrifugation after each cycle was employed in the subsequent cycle with an identical concentration of dye solution. Fig. 10a displays the photodegradation findings for all cycles.

The effectiveness of photocatalytic degradation decreased from 98.99% to 96.7% over six cycles, attributed to the partial obstruction of active sites by intermediate intermediates. The little decline of 2.31% after six cycles demonstrates the exceptional reusability and photostability of the CuS/CdS photocatalyst. X-ray diffraction analysis was utilized to assess the structural integrity of the CuS/CdS heterostructure prior to and during its photocatalytic activity. Fig. 10b displays the XRD spectra for CuS/CdS before and after activity. Following five consecutive photocatalytic cycles, the photocatalyst retained all its unique X-ray diffraction peaks, indicating exceptional structural integrity and stability.[47]

3.8. Scavenging experiments and associated mechanism

Photocatalytic degradation experiments against the trypan blue were conducted in the presence of various scavengers to investigate the contribution of different reactive oxygen species in dye degradation. Fig. 11a presents the effect of scavengers like isopropanol (˙OH quencher), sodium nitrate (e^- quencher), ethylenediaminetetraacetic acid (h^+ quencher), p-benzoquinone (˙O_2^- quencher) on the degradation rate constant.

The degradation rate constant without any scavenger was found to be $0.039 \ min^{-1}$. The dye degradation rate constant decreased from $0.039 \ min^{-1}$ to $0.019 \ min^{-1}$, $0.022 \ min^{-1}$, $0.028 \ min^{-1}$ and $0.011 \ min^{-1}$ in the presence of isopropanol, sodium nitrate, ethylenediaminetetraacetic acid (EDTA) and p-benzoquinone (PBQ) respectively. Hence, electrons and holes can be classified as minor contributors, and the hydroxyl radical (˙OH) is moderate contributor. Conversely, the superoxide radical (˙O_2^-) is the principal agent responsible for dye degradation activity. The photoactivity of the CuS/CdS heterojunction is principally governed by the positions of the VB and CB, which regulate the mobility of holes and electrons as well as the formation of reactive oxygen species during the photoreaction. The edge potentials of the conduction and valence bands (E_{CB}; E_{VB}) were calculated using the subsequent equations:[48]
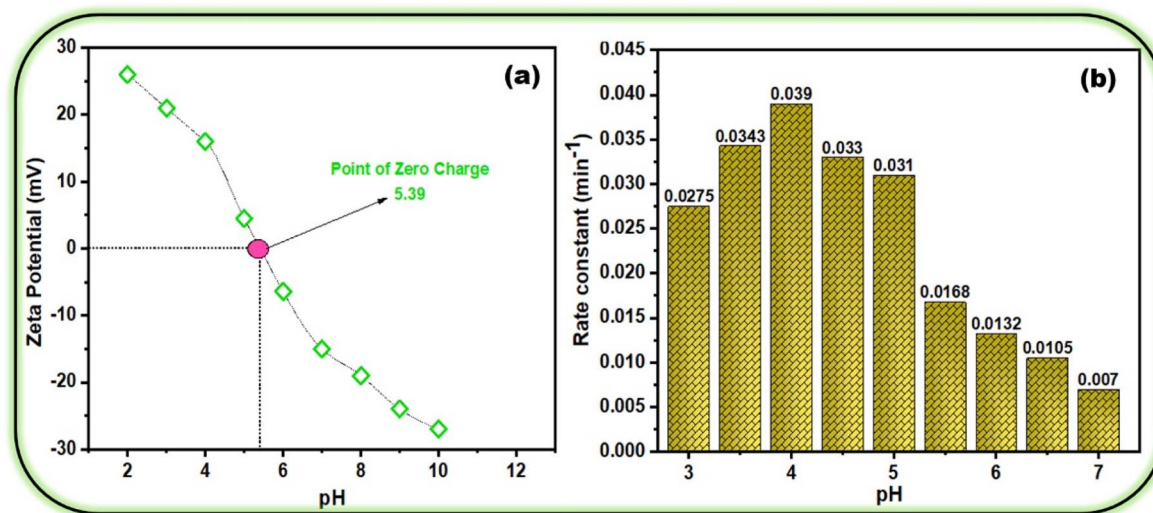

Fig. 9 (a) Point of zero charge for CuS/CdS composite; (b) effect of pH on the dye degradation efficiency of CuS/CdS composite.
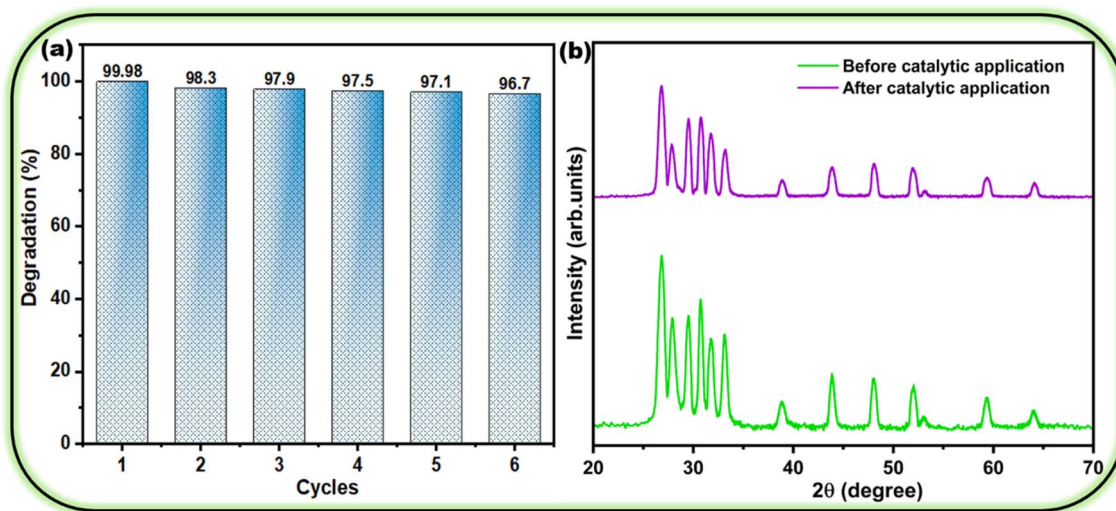
Fig. 10 (a) Recyclability assessment of the CuS/CdS composite through repeated photocatalytic cycles, and (b) XRD patterns of the composite before and after photocatalytic treatment to evaluate structural stability.
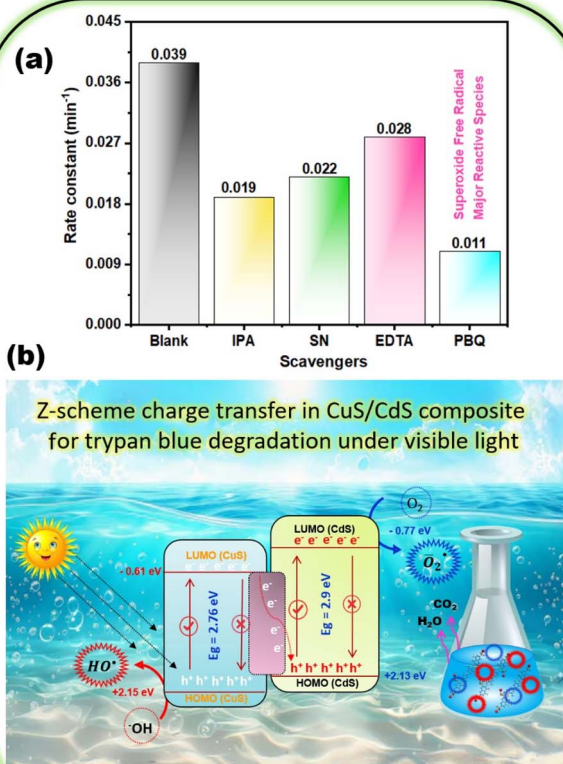

Fig. 11 (a) Scavenging experiments and (b) the suggested degradation pathway of trypan blue.

$$E_{CB} = \chi - E_e - 0.5E_g \qquad (5)$$

$$E_{VB} = E_g + E_{CB} \qquad (6)$$

'χ' is the semiconductor's electronegativity, 'E_e' the free electron energy (4.5 eV vs. NHE), and 'E_g' the bandgap energy. The conduction and valence band potentials were found to be −0.77 eV and +2.13 eV for CdS, and −0.61 eV and +2.15 eV for CuS, respectively (Fig. 11b). When exposed to visible light, both semiconductors can absorb photons and generate electron–hole pairs. The favourable band alignment and interfacial internal electric field of the heterojunction facilitate the transport of electrons from the CB of CuS to the VB of CdS, resulting in recombination with photogenerated holes. The efficient separation of charge carriers is facilitated by the Z-scheme charge transfer mechanism, which leads to the accumulation of electrons in the CB of CdS and holes in the VB of CuS. The conduction band of CdS (−0.77 eV) is more negative than the reduction potential of molecular oxygen to superoxide radicals ($^\bullet O_2^-$, $E^0 = -0.33$ eV).[49] In contrast, the VB of

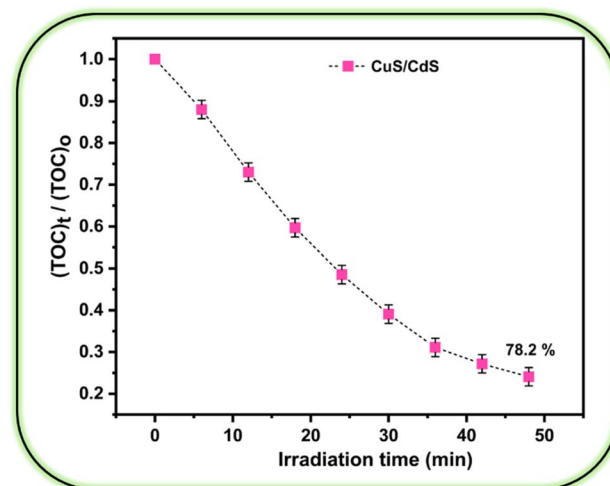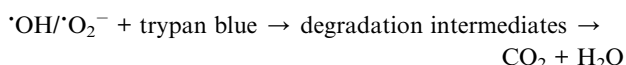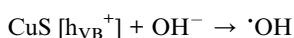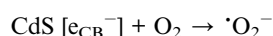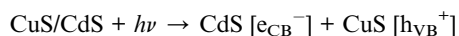Fig. 12 Normalized TOC vs. time for trypan blue (15 mg L^{-1}) over CuS/CdS under visible light.

CuS (+2.15 eV) is situated above the potential required for hydroxide ion oxidation ($OH^-/{}^\bullet OH$, +1.99 eV), hence enabling the generation of hydroxyl radicals (${}^\bullet OH$).[50] The valence band is somewhat below the potential for direct water oxidation (+2.38 eV) to hydroxyl radicals, rendering it unfeasible.

Furthermore, the internal electric field produced by the p–n junction at the interface can enhance the directional mobility of charge carriers, impede recombination, and promote the formation of reactive oxygen species (ROS). The resulting superoxide radicals and hydroxyl radicals are responsible for the reductive and oxidative degradation of TBD, respectively. The photodegradation products of TBD are simple, harmless molecules of water and carbon dioxide.

The possible reactions involved in the dye degradation are written below:[51]

$$CuS/CdS + h\nu \rightarrow CdS\,[e_{CB}^-] + CuS\,[h_{VB}^+]$$

$$CdS\,[e_{CB}^-] + O_2 \rightarrow {}^\bullet O_2^-$$

$$CuS\,[h_{VB}^+] + OH^- \rightarrow {}^\bullet OH$$

$$^\bullet OH/{}^\bullet O_2^- + \text{trypan blue} \rightarrow \text{degradation intermediates} \rightarrow$$
$$CO_2 + H_2O$$

3.9. TOC validation of mineralization

To unambiguously distinguish apparent decolorization from genuine mineralization, we performed time-resolved TOC measurements on trypan blue solutions photocatalyzed by CuS/CdS under visible-light irradiation. As evident form Fig. 12, the normalized TOC declined monotonically, reaching 78.2% removal at 48 min, closely paralleling the 81% trypan blue decolorization measured under identical conditions. The small TOC–absorbance offset indicates that chromophore cleavage slightly precedes complete mineralization; the residual TOC most likely reflects short-lived, partially oxidized fragments and minor surface-retained species rather than adsorption artifacts (samples were dark-equilibrated before irradiation). Collectively, the TOC kinetics substantiate genuine mineralization in the CuS/CdS system and align with a two-stage pathway—rapid de-azo cleavage followed by slower ring-opening and stepwise oxidation to CO_2/H_2O—supported by efficient charge separation in the direct Z-scheme heterojunction.

4. Conclusion

In summary, a CuS/CdS heterojunction was synthesized *via* a straightforward co-precipitation approach followed by annealing for photodegradation of toxic dyes and other pollutants in the water systems. The characterization techniques, such as XRD, EDX, SEM, FTIR, UV-Vis, transient photocurrent, and *I–V* measurements, were used for investigating structural, compositional, morphological, functional, optical, and electrical features of fabricated samples. In the application study, the photocatalytic performance of the CuS/CdS composite was evaluated for the degradation of trypan blue dye. The CuS/CdS composite exhibited 100% dye removal (with 19% sorption and 81% photodegradation) within the irradiation period of 48 minutes. At the same time, the pristine CuS and CdS demonstrated only 74.9% and 56.5% dye removal for 48 minutes under the same reaction conditions. The observed rate constant for the CuS/CdS composite (0.039 min^{-1}) was 2.79 times greater than that of CdS (0.014 min^{-1}) and 1.86 times more than that of CuS (0.021 min^{-1}). The improved surface area, reduced band gap, and formation of a p–n junction between CuS and CdS enhance dye absorption maximize visible light utilization, and suppress charge recombination, thereby contributing to the superior performance of the composite compared to its pristine components. The results revealed the CuS/CdS composite to be an effective, long-lasting photocatalyst with great promise for real-world environmental remediation applications.

Author contributions

Samina Kousar (write up of the manuscript and experimental work), Mohamed Abdel Rafea (methodology, funding acquisition, and resources), Magdi E. A. Zaki (project administration and formal analysis), M. Khairy (data curation), Mohamed R. El-Aassar (visualization and data curation), Abdullah K. Alanazi (conceptualization and formal analysis), Imran Shakir (editing and proof reading and formal analysis), Sidra Mubeen (co-supervision and data curation), Muhammad Aadil (supervision).

Conflicts of interest

The authors declare that they have no known competing financial interests or personal relationships that could have appeared to influence the work reported in this paper.

Data availability

Data will be available upon request.

Acknowledgements

References

1 S. Xie, J. Jiang, G. Zhou, Y. Chen, A. Zhang, X. Xia, M. Shi, B. Deng, C. Yu and H. He, Optimizing electronic structure through lattice engineering for enhanced photocatalytic reduction of Cr(VI), *Inorg. Chem. Commun.*, 2025, **173**, 113845.

2 D. A. Islam, G. M. Choudhury and H. Acharya, Layered double hydroxide (LDH)-derived zinc oxide (ZnO) nanorod on exfoliated graphene oxide (GO) nanosheet for photocatalytic dye degradation and hexavalent chromium reduction, *J. Solid State Chem.*, 2024, **336**, 124776.

3 H. A. Alsalmah, Green synthesis of copper doped bismuth oxide: A novel inorganic material for photocatalytic mineralization of Trypan blue dye, *Inorg. Chem. Commun.*, 2024, **163**, 112270.

4 H. Wu, L. Li, S. Wang, N. Zhu, Z. Li, L. Zhao and Y. Wang, Recent advances of semiconductor photocatalysis for water pollutant treatment: mechanisms, materials and applications, *Phys. Chem. Chem. Phys.*, 2023, **25**, 25899–25924.

5 P. Chen, Y. Zhai, Y. Bao and S. Zhu, Recent Advances and Applications of Modified-Semiconductor Photocatalyst in Pollutant Degradation, *Advances in Catalysts Research*, 2024, pp. 171–219.

6 H. He, W. Peng, J. Jiang, X. Xia, J. Luo, S. Luo, X. Wang, K. Yang and C. Yu, Surface modifying $ZnWO_4$ with Zn QDs and oxygen vacancies for enhanced photocatalytic Cr(VI) reduction, *Colloids Surf., A*, 2025, **723**, 137420.

7 Y. Zhu, Y. Liu, Q. Ai, G. Gao, L. Yuan, Q. Fang, X. Tian, X. Zhang, E. Egap and P. M. Ajayan, In situ synthesis of lead-free halide perovskite–COF nanocomposites as photocatalysts for photoinduced polymerization in both organic and aqueous phases, *ACS Mater. Lett.*, 2022, **4**, 464–471.

8 J. Naseem, M. A. Rafea, M. E. A. Zaki, M. I. Attia, M. R. El-Aassar, F. Alresheedi, S. Zulfiqar and M. Aadil, Combining nanotechnology and nanohybrid methods to improve the physical and chemical properties of CuS and boost its photocatalytic aptitude, *RSC Adv.*, 2025, **15**, 13940–13950.

9 C. Yang, C. Qing, Q. Wang, X. Zhang, J. Lou and Y. Liu, Synthesis of the hybrid CdS/Au flower-like nanomaterials and their SERS application, *Sens. Actuators, B*, 2020, **304**, 127218.

10 W. Wang, J. Xue and J. Liu, Recent advances in CdS heterojunctions: morphology, synthesis, performances and prospects, *J. Mater. Chem. A*, 2024, **12**, 10659–10675.

11 C. Q. Li and J. J. Wang, Copper sulfide based photocatalysts, electrocatalysts and photoelectrocatalysts: Innovations in structural modulation and application, *Small*, 2024, **20**, 2404798.

12 A. Balapure, J. R. Dutta and R. Ganesan, Recent advances in semiconductor heterojunctions: a detailed review of the fundamentals of photocatalysis, charge transfer mechanism and materials, *RSC Appl. Interfaces*, 2024, **1**, 43–69.

13 Y. Song, X. Zheng, Y. Yang, Y. Liu, J. Li, D. Wu, W. Liu, Y. Shen and X. Tian, Heterojunction engineering of multinary metal sulfide-based photocatalysts for efficient photocatalytic hydrogen evolution, *Adv. Mater.*, 2024, **36**, 2305835.

14 B. Zhu, J. Sun, Y. Zhao, L. Zhang and J. Yu, Construction of 2D S-scheme heterojunction photocatalyst, *Adv. Mater.*, 2024, **36**, 2310600.

15 S. K. Sahoo, L. Acharya, L. Biswal, P. Priyadarshini and K. Parida, Recent advancements in graphitic carbon nitride based direct Z- and S-scheme heterostructures for photocatalytic H_2O_2 production, *Inorg. Chem. Front.*, 2024, **11**, 4914–4973.

16 J. Li, H. Yuan, W. Zhang, B. Jin, Q. Feng, J. Huang and Z. Jiao, Advances in Z-scheme semiconductor photocatalysts for the photoelectrochemical applications: a review, *Carbon Energy*, 2022, **4**, 294–331.

17 X. She, J. Wu, H. Xu, J. Zhong, Y. Wang, Y. Song, K. Nie, Y. Liu, Y. Yang, M.-T. F. Rodrigues, R. Vajtai, J. Lou, D. Du, H. Li and P. M. Ajayan, High Efficiency Photocatalytic Water Splitting Using 2D α-Fe_2O_3/g-C_3N_4 Z-Scheme Catalysts, *Adv. Energy Mater.*, 2017, **7**, 1700025.

18 S. Alikarami, A. Soltanizade and F. Rashchi, Photocatalytic activity of the visible-light-driven spherical Ag_2S modifying the CdS synthesized by the facile chemical methods for the degradation of methylene blue and rhodamine B, *Mater. Chem. Phys.*, 2022, **285**, 126174.

19 K. Wen, L. Wei, Z. Ren, B. Wang and J. Lu, Enhanced photocatalytic degradation of cationic and anionic dyes by Ag-modified g-C_3N_4 composite: Insights on different mechanisms under visible light, *J. Mater. Res.*, 2021, **36**, 1549–1560.

20 Y. Liu, X. Zheng, Y. Yang, J. Li, W. Liu, Y. Shen and X. Tian, Photocatalytic hydrogen evolution using ternary-metal-sulfide/TiO_2 heterojunction photocatalysts, *ChemCatChem*, 2022, **14**, e202101439.

21 Y. Chen, X. Wang, B. Liu, Y. Zhang, Y. Zhao and S. Wang, Directional regulation of reactive oxygen species in titanium dioxide boosting the photocatalytic degradation performance of azo dyes, *J. Colloid Interface Sci.*, 2024, **673**, 275–283.

22 H. Sabeeh, M. Aadil, S. Zulfiqar, A. Rasheed, N. F. Al-Khalli, P. O. Agboola, S. Haider, M. F. Warsi and I. Shakir, Hydrothermal synthesis of CuS nanochips and their nanohybrids with CNTs for electrochemical energy storage applications, *Ceram. Int.*, 2021, **47**, 13613–13621.

23 N. AttariKhasraghi, K. Zare, A. Mehrizad, N. Modirshahla and M. A. Behnajady, Achieving the enhanced photocatalytic degradation of ceftriaxone sodium using CdS-gC_3N_4 nanocomposite under visible light irradiation: RSM modeling and optimization, *J. Inorg. Organomet. Polym. Mater.*, 2021, **31**, 3164–3174.

24 R. Sreedhara, B. R. Krushna, S. Sharma, N. R. Nadar, C. Krithika, F. D. Joy, V. Shivakumar, S. Devaraja, K. Manjunatha and T.-E. Hsu, Straightforward green synthesis of Fe^{3+} doped $ZnAl_2O_4$ spinel structure and potential applications in alleviating thrombosis, oxidative stress, data encryption and dermatoglyphics, *Surf. Interfaces*, 2024, **46**, 104005.

25 N. Singh, S. Chand and M. Taunk, Facile in-situ synthesis, microstructural, morphological and electrical transport properties of polypyrrole-cuprous iodide hybrid nanocomposites, *J. Solid State Chem.*, 2021, **303**, 122501.

26 N. Chandran, R. Malavika, M. Bayal, R. Pilankatta and S. S. Nair, CuS-Cu hybrid nanostructures and their applications in electrochemical sensing of homocysteine, *Surf. Interfaces*, 2024, **44**, 103769.

27 A. K. Chitoria, A. Mir and M. Shah, A review of ZrO_2 nanoparticles applications and recent advancements, *Ceram. Int.*, 2023, **49**, 32343–32358.

28 Z. You, D. Lu, K. K. Kondamareddy, W. Gu, Y. Su, J. Pan, J. Yang, P. Cheng and W. Ho, Organic-inorganic PVDF/ $Zn_{0.5}Cd_{0.5}S$/Ti-NT photocatalytic membrane with synergistic effect of heterojunction and its derived multi-element excitation NO purification, *Sep. Purif. Technol.*, 2025, **361**, 131293.

29 R. H. Alshammari, M. Aadil, T. Kousar, U. Maqbool, Z. Ahmad, A. M. Alswieleh, T. S. Algarni and M. Naeem, Synthesis of Binary Metal Doped CuO Nanoarchitecture for Congo red dye Removal: Synergistic Effects of Adsorption and Mineralization Techniques, *Opt. Mater.*, 2023, **144**, 114314.

30 J. Feng, Y. Lu, H. Xie, Y. Zhang, S. Huo, X. Liu, M. Flynn, Z. Xu, P. Burey and M. Lynch, Atom-economic synthesis of an oligomeric P/N-containing fire retardant towards fire-retarding and mechanically robust polylactide biocomposites, *J. Mater. Sci. Technol.*, 2023, **160**, 86–95.

31 Z. Xu, Z. Feng and Y. Xu, Preparation and characterization of R_2CoMnO_6 (R = La, Nd) via PVA sol-gel route, *J. Asian Ceram. Soc.*, 2021, **9**, 142–150.

32 R. Tariq, S. Zulfiqar, H. H. Somaily, M. F. Warsi, I. Ayman, F. Hanif, M. Akhtar and M. Aadil, Synthesis of carbon supported iron oxide nanochips and their composite with glutathione: A novel electrochemical sensitive material, *Surf. Interfaces*, 2022, **34**, 102350.

33 A. Q. Malik, S. Sena, D. Kumar, M. Wani and A. Rashid, Assessment of photocatalytic efficiency and antifungal activity of zinc doped copper sulfide composite embedded with graphene oxide nanosheets, *J. Mol. Liq.*, 2024, **395**, 123925.

34 B. Qasim, K. Jabbour, M. Ouladsmane, M. S. Waheed, M. Abdullah, N. Bano, S. Manzoor, M. Sillanpää and M. N. Ashiq, Effect of Ni dopant on the capacitive behavior of CuS for supercapacitor application, *J. Mater. Sci.: Mater. Electron.*, 2024, **35**, 445.

35 A. Al Busaidi, F. Al Marzouqi, A. T. Kuvarega, M. Sillanpaa and R. Selvaraj, Bimetallic $Cd_xZn_{(1-x)}O$ photocatalytic material for the degradation of levofloxacin under solar light irradiation, *Inorg. Chem. Commun.*, 2023, **151**, 110573.

36 M. M. El-Sheekh, W. E. Yousuf, E.-R. Kenawy and T. M. Mohamed, Biosynthesis of cellulose from *Ulva lactuca*, manufacture of nanocellulose and its application as antimicrobial polymer, *Sci. Rep.*, 2023, **13**, 10188.

37 X. Zhao, J. Dong, Y. Fang, J. Dai, J. Chen, X. Song, Z. Fu, W. Sun, Q. Wang and Z. Yan, Cu_2O@Au-CsPbI$_3$ heterostructures for plasmon hot carrier transfer enhanced optoelectronics, *J. Alloys Compd.*, 2024, **981**, 173644.

38 A. Naz, I. Bibi, F. Majid, A. Dahshan, K. Jilani, B. Taj, A. Ghafoor, Z. Nazeer, F. M. Alzahrani and M. Iqbal, Cu and Fe doped $NiCo_2O_4$/g-C_3N_4 nanocomposite ferroelectric, magnetic, dielectric and optical properties: visible light-driven photocatalytic degradation of RhB and CR dyes, *Diamond Relat. Mater.*, 2024, **141**, 110592.

39 N. U. A. Khakwani, M. Aadil, I. Barsoum, Z. Ahmad, G. M. Kamal, M. R. Karim, A. A. Alothman and M. F. Warsi, Tailoring the physical, optical, and structural properties of bismuth oxide to enhance its anionic,

40 R. Gupta, S. Singh, R. Walia, V. Kumar and V. Verma, Modification in photovoltaic and photocatalytic properties of bismuth ferrites by tailoring band-gap and ferroelectric properties, *J. Alloys Compd.*, 2022, **908**, 164602.

cationic, and phenol dye degradation activities, *Ceram. Int.*, 2024, **50**, 33333–33344.

41 H. He, Z. Luo and C. Yu, Embellish zinc tungstate nanorods with silver chloride nanoparticles for enhanced photocatalytic, antibacterial and antifouling performance, *Colloids Surf., A*, 2021, **613**, 126099.

42 A. Das, M. Patra, M. Bhagavathiachari and R. G. Nair, Role of type II heterojunction in ZnO–In$_2$O$_3$ nanodiscs for enhanced visible-light photocatalysis through the synergy of effective charge carrier separation and charge transport, *Mater. Chem. Phys.*, 2021, **263**, 124431.

43 Y. Wang, X. Chen and C. Chen, Microwave synthesis of Zn, Cd binary metal sulfides with superior photocatalytic H$_2$ evolution performance, *Inorg. Chem. Commun.*, 2021, **134**, 108993.

44 Z. Xie, R. Yu, Z. Huang, H. Qiao and X. Qi, Photoelectrochemical Photodetectors Based on WSe$_2$/rGO Hybrid Structure with Enhanced Performance, *J. Electron. Mater.*, 2024, **53**, 6974–6985.

45 Y. Zhao, Y. Zuo, G. He, Q. Chen, Q. Meng and H. Chen, Synthesis of graphene-based CdS@CuS core-shell nanorods by cation-exchange for efficient degradation of ciprofloxacin, *J. Alloys Compd.*, 2021, **869**, 159305.

46 M. S. Rohokale, D. Dhabliya, T. Sathish, V. Vijayan and N. Senthilkumar, A novel two-step co-precipitation approach of CuS/NiMn$_2$O$_4$ heterostructured nanocatalyst for enhanced visible light driven photocatalytic activity via efficient photo-induced charge separation properties, *Phys. B*, 2021, **610**, 412902.

47 B. A. Alwan, M. Aadil, F. Alresheedi, A. Alazmi, A. El Jery, M. R. Alrahili, M. Algarni, M. R. El-Aassar and T. Alomayri, Assembly of coral-like delafossite-structured AgFeO$_2$ with a polypyrrole framework for improved photocatalytic treatment of trypan blue dye, *J. Alloys Compd.*, 2025, **1011**, 178361.

48 K. Karami, S. M. Beram, F. Siadatnasab, P. Bayat and A. Ramezanpour, An investigation on MIL-101 Fe/PANI/Pd nanohybrid as a novel photocatalyst based on MIL-101(Fe) metal–organic frameworks removing methylene blue dye, *J. Mol. Struct.*, 2021, **1231**, 130007.

49 E. B. Simsek and Ö. Tuna, Understanding the nature of Ce–Fe synergy in the structure CaWO$_4$ scheelite for enhanced photocatalytic performance under visible light, *Ceram. Int.*, 2024, **50**, 20600–20611.

50 Y. Wang, Z. Zhang, Y. Chen, Z. Zhu, H. Wang and X. Tang, Enhanced LED light-driven antibacterial system with efficient charge transfer coordinated by Bi$_2$WO$_6$/TiO$_2$ Z-scheme heterojunction, *Ceram. Int.*, 2024, **50**, 9307–9322.

51 J. R. Rajabathar, R. Thankappan, A. Sutha, H. Al-Lohedan, A. Mahmoud Karami, S. Ashok Kumar, G. Devendrapandi, S. Roji Marjorie and R. Balu, Enhanced photocatalytic activity of magnetite/titanate (Fe$_3$O$_4$/TiO$_2$) nanocomposite for methylene blue dye degradation under direct sunlight, *Opt. Mater.*, 2024, **148**, 114820.